Eur. Phys. J. A **3**, 149–157 (1998)

THE EUROPEAN PHYSICAL JOURNAL A

Light charged particle emission induced by neutrons with energies between 25 and 65 MeV on oxygen. I. Protons and deuterons

S. Benck[1], I. Slypen[1], J.P. Meulders[1], V. Corcalciuc[2]

[1] Institut de Physique Nucléaire, Université Catholique de Louvain, Chemin du Cyclotron 2, B-1348 Louvain-la-Neuve, Belgium
[2] Institute for Atomic Physics, PO Box MG6, Bucharest, Romania

Received: 24 April 1998 / Revised version: 1 July 1998
Communicated by D. Schwalm

Abstract. Double-differential cross sections (energy spectra) for proton and deuteron emission in fast neutron induced reactions on oxygen are reported for nine incident neutron energies between 25 and 65 MeV. Angular distributions were measured at 15 laboratory angles between 20° and 160°. Procedures for data taking and data reduction are presented. Deduced energy-differential, angle-differential and total cross sections are also reported. Experimental cross sections are compared with existing data and with theoretical model calculations.

PACS. 25.40.-h Nucleon-induced reactions – 25.40.Hs Transfer reactions – 28.20.-v Neutron physics

1 Introduction

Experimental measurements of charged particle production for fast neutron induced reactions in the incident energy range 30 to 80 MeV are rather scarce [1,2]. The present paper reports measurements of proton and deuteron inclusive emission spectra at nine incident neutron energies on oxygen, in the range 25 to 65 MeV. Experimental data were obtained at the fast neutron facility at the Louvain-la-Neuve cyclotron, CYCLONE. Previous results for neutron induced light charged particle production on carbon in the energy interval 40–75 MeV were reported by our group [3, 4].

Experimental results concerning light charged particle production in proton induced reactions on oxygen at comparable incident energies: 28.8, 39.0 and 61.5 MeV, are available [5]. Our data, together with those of [5], provide complementary information on nucleon induced light charged particle emission. This allows a comparison of the influence of the projectile isospin on the relative magnitudes of charged particle yields and facilitates more detailed tests of nuclear models.

In addition to basic physics interest, neutron induced reactions above 20 MeV are important in a number of new accelerator based technologies as for example the transmutation of radioactive waste. Besides, in the case of light target nuclei (carbon, oxygen), a detailed knowledge of cross sections allows to evaluate the contribution of a given element as a constituent of human tissue or neutron detector [6, 7].

We report here double-differential cross sections and their angular distributions for proton and deuteron emission from oxygen at 28.5 ± 1.5, 31.5 ± 1.5, 34.5 ± 1.5, 37.5 ± 1.5, 41.0 ± 2.0, 45.0 ± 2.0, 49.0 ± 2.0, 53.5 ± 2.5 and 62.7 ± 2.0 MeV incident neutron energies. Measurements were done at 15 laboratory angles between 20° and 160° in steps of 10° lab.

In Sec. 2, the experimental set-up is briefly described. Data reduction procedures including normalisation and corrections to the measured spectra are presented in Sec. 3. Experimental results and theoretical calculations are shown in Sec. 4. Conclusions are covered in Sec. 5.

2 Experimental set-up

Figure 1 shows the general lay-out (not at scale) of the fast neutron beam facility at the Louvain-la-Neuve Cyclotron, CYCLONE, previously described in detail [8–10]. The 65 MeV incident proton beam is focused on a 3 mm thick natural lithium target. With a beam intensity of 10^{-5} A, about 10^6 n/s are available at the location of our reaction chamber (around 3.3 m downstream the lithium target). The neutron energy spectrum at 0° consists of a well-defined peak (2 MeV full-width-at-half-maximum) containing about 50% of the neutrons, plus a flat continuum of low energy neutrons [1, 10]. In the main neutron peak there are about 10 times more neutrons/MeV than in the low neutron energies continuum.

The evacuated reaction chamber (406 mm in diameter) can be turned in the reaction plane and has ten ports to

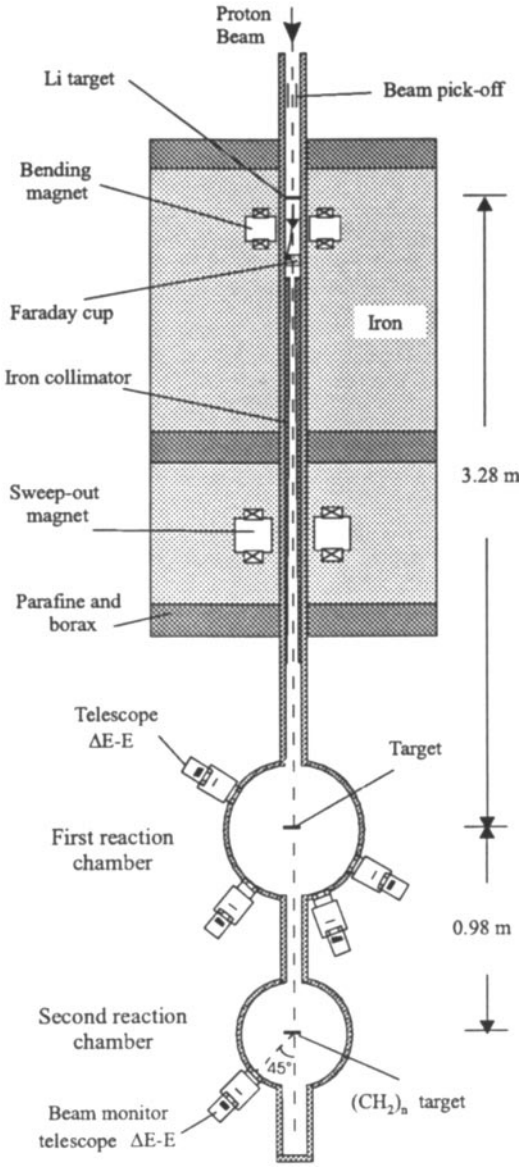

Fig. 1. General lay-out of the fast neutron facility (not at scale) at the Louvain-la-Neuve cyclotron

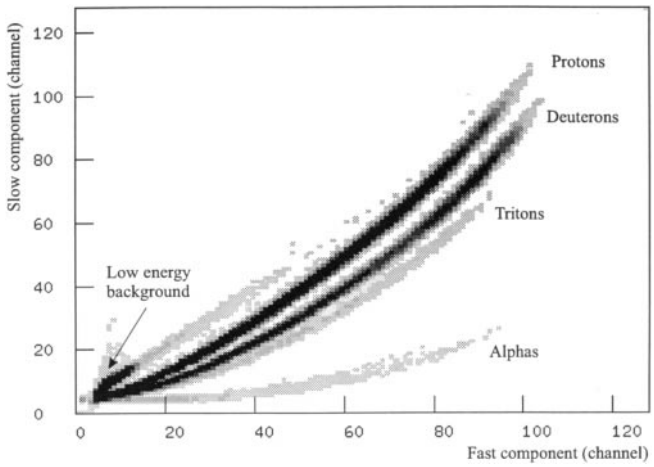

Fig. 2. Particle discrimination spectrum taken at 20° with an Al_2O_3 target, in slow vs fast relation, before low energy background elimination

accommodate the holding system of the telescopes. Angles from 20° to 160° in steps of 10° are available.

Four charged particle detector telescopes were used simultaneously. Each of them consists of: i) a ΔE detector (NE102 plastic scintillator, 0.1 mm thick, 4 cm in diameter) viewed by a XP2020 photomultiplier via a lucite light guide, and ii) of an E detector (CsI(Tl) crystal, 22 mm thick, 38.1 mm in diameter), viewed by a XP2262B photomultiplier. The E detector can stop 80 MeV protons. A coincidence is required between ΔE and E detectors in order to suppress an important part of the background present in such type of experiments.

For the oxygen measurements two targets were used in successive runs: an elemental Al and an Al_2O_3 target, both of 5×5 cm^2 surface and 1 mm thick. The angle of the target with the beam was chosen to minimise the thickness of the target material traversed by the produced charged particles towards the detector telescopes.

For energy calibration, the protons and deuterons recoiling respectively from a 1 mm thick polypropylene and a 0.6 mm thick deuterated polypropylene target were used. They were recorded at laboratory angles from 20° to 70° in steps of 10°, for each of the four telescopes. The H(n,p) scattering is registered with good statistics, for a precise determination of differential cross-sections to be subsequently used as reference cross-sections.

Charged particle discrimination spectra were obtained in two ways: i) by using the energy information from ΔE−E telescopes and ii) by charge integration of the CsI light output pulse [10–12]. In the latter case, the signal is integrated during a fast gate (600 ns width) and a slow gate (2700 ns width). A combined use of the two separation methods [10], allows a reliable low energy background elimination and a very good separation of the reaction products over their entire energy range. Figure 2 shows a particle separation spectrum in slow vs. fast component display, taken on Al_2O_3 target at 20°, before the elimination of the low energy background.

The beam monitoring system (Fig. 1) is realised in two ways: i) behind the lithium target, the incident proton beam is deflected by a magnetic dipole and integrated into a water cooled Faraday cup and ii) downstream our reaction chamber and coupled to it, there is a second evacuated chamber in which a 1 mm thick polypropylene target is placed perpendicular to the neutron beam. A charged particle telescope (2 mm thick NE102 scintillator as ΔE and a CsI(Tl) crystal as E detector) detects at 45° the H(n,p) scattered protons. The integral of the recoil proton peak serves as a second monitor during the measurements. The two monitoring systems were in very good agreement during the experiment.

For each charged particle event in a telescope, a time-of-flight (TOF) between a capacitive beam pick-off located upstream of the neutron producing target (Fig. 1) and the ΔE detector is registered, and subsequently used to select

only those events associated with the incident neutrons in a desired energy interval. The time resolution in the experiment was 0.8 ns.

3 Data reduction

Details about procedures adopted for data reduction are given elsewhere [10, 13].

Once a reaction product is selected in Fig. 2, by complementary use of $\Delta E - E$ and slow vs. fast information in the particle discrimination spectra, a reliable selection of the desired events is obtained over their entire energy range [10]. Subsequently, using TOF information and knowing the involved flight distances and energies of the particles (from the energy calibration), the incident neutron energy spectrum, inducing the chosen charged particle ejectiles, is reconstructed. Figure 3 shows a deuteron spectrum taken at 20° lab with an Al target. A further selection is then done of only those charged particle events induced by the desired incident neutron energies. As an example, Fig. 3 shows the selection of deuteron events induced by neutrons in the main neutron peak (hatched area) respectively neutrons of 41.0 ± 2.0 MeV energy (dotted area). The statistics in our oxygen double-differential spectra correspond to an acquisition time of about 52 h for each of the targets, with about 12×10^{-6} A mean proton beam on the 3 mm thick lithium target.

Absolute cross sections are obtained by normalisation to our measured H(n,p) scattering cross-sections [14]. With each of the four telescopes, angular distributions for the n-p elastic scattering were measured at 6 laboratory angles between 20° and 70°. Therefore, for each of the telescopes, six normalisation points are available, covering a large energy range, and the normalisation factor was a mean value of them. Generally, the spread of these values around their mean was about 5%. Normalisation factors of the order 3.5×10^{-4} mb/MeVsr are obtained for charged particle events induced by neutrons in the high energy peak. Considering 10 counts in a 2 MeV ejectile energy bin we get an inferior detection limit of about 3.5×10^{-3} mb/MeVsr corresponding to 33% statistical error. For data obtained at incident neutron energies from the flat continuum of the incident neutron energy spectra, this limit becomes 3.5×10^{-2} mb/MeVsr due to the fact that there are about 10 times less neutrons in an low incident neutron energy bin than in the main peak.

The rather thick targets used, the 0.1 mm thick ΔE detector and the threshold of the E detector will limit the registration of the low energy charged particle products to only fractions of the entire target thickness, therefore the spectra should be accordingly corrected. Solid angles and thick target corrections are calculated by a Monte Carlo simulation programme of the experiment [15]. The programme includes energy losses in the target material and the ΔE detector, the threshold of E detectors (about 1.5 MeV in our measurement), kinematics of the reaction, neutron beam energy width, neutron beam profile, geometry target-detector and geometry of the collimating system of the telescopes. The collimation of each charged particle detector telescope, had an angular opening between 2° and 3°. The calculated thick target correction factors are mean values over the energy spread introduced by the target material and ΔE detector, for each of the charged particle products. For our Al or Al_2O_3 targets and the specified characteristics of $\Delta E - E$ telescopes, these corrections start from around 17 MeV proton and 23 MeV deuteron energy down to the low energy cuts in the spectra. These limits are influenced by the target-telescope relative angle [15].

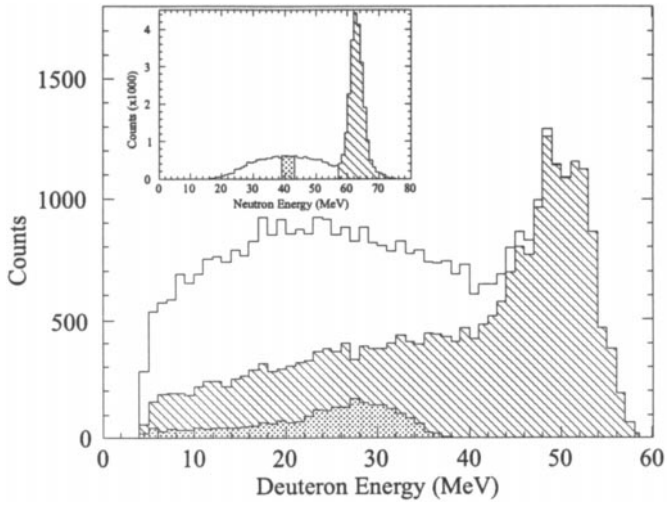

Fig. 3. Selection of deuteron events induced by two incident neutron energies: 62.7 MeV – main peak (hatched area) and 41.0 ± 2.0 MeV from the continuum (dotted area). In the insert, the incident neutron energy spectrum reconstructed from all deuteron events is presented

4 Results and discussion

Following the procedures outlined above, double-differential cross-sections ($d^2\sigma/d\Omega dE$) and their angular distributions at 15 laboratory angles between 20° and 160° for proton and deuteron production were obtained for nine incident neutron energies: 28.5 ± 1.5, 31.5 ± 1.5, 34.5 ± 1.5, 37.5 ± 1.5, 41.0 ± 2.0, 45.0 ± 2.0, 49.0 ± 2.0, 53.5 ± 2.5 and 62.7 ± 2.0 MeV. Low energy cuts are around 6 MeV for protons and 8 MeV for deuterons, given by the thickness of the target and the ΔE detector and the energy threshold of the E detector.

The overall relative errors of the points in the spectra are about 5% for protons and 9% for deuterons for 62.7 MeV data, 14% for protons and 22% for deuterons for all the other incident neutron energies. They are given by the statistics in the spectra except for lower ejectile energies where they can be bigger due to thick target corrections [15].

The uncertainty of the cross section absolute scale is about 7–8%, given by errors in the measured reference (n,p) cross-sections (5%), beam monitoring (2%), statistics in the H(n,p) recoil proton peak (2–5%), solid angle corrections (1%), number of target nuclei (1%) etc.

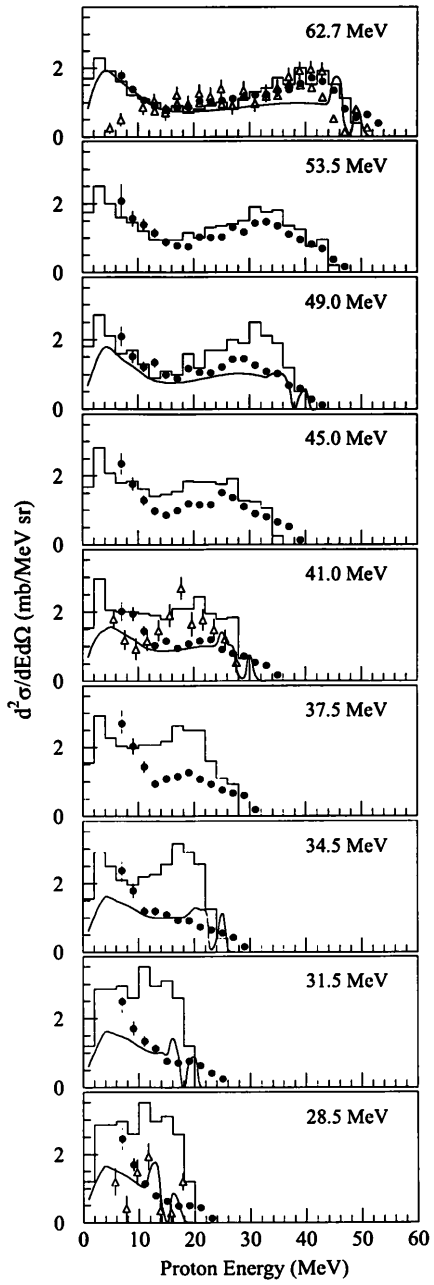

Fig. 4. Double-differential cross sections ($d^2\sigma/d\Omega dE$) for ^{16}O(n,px) reactions at 20° lab, for the nine indicated incident neutron energies. Filled dots represent data, in steps of 2 MeV, of this work. Similar experimental data [16] are shown as triangles. Intranuclear cascade model calculations [17] are presented as histograms while GNASH calculations [20] as continuous lines

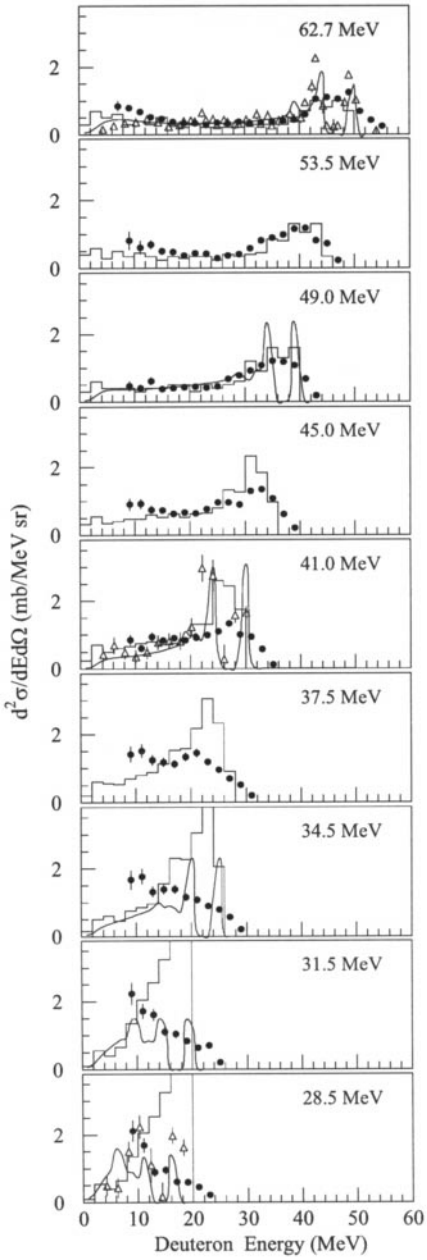

Fig. 5. Same as in Fig. 4 for the case of ^{16}O(n,dx) reactions

Experimental double-differential cross sections in neutron induced reactions on oxygen at 27.4, 39.7 and 60.7 MeV were previously published [16]. Measurements were done for the angular distributions only at forward angles (less than 70° lab). The chosen incident neutron energies in [16] are the same as those of [5] for proton induced reactions on oxygen.

Figs. 4, 5 show 20° laboratory angle double-differential cross sections for respectively the ^{16}O(n,px) and the ^{16}O(n,dx) reactions vs incident neutron energy. The data of the present work are shown as filled dots in 2 MeV steps with their respective errors. For comparison, at 62.7, 41.0 and 28.5 MeV incident neutron energies, the experimental data of [16] are also presented (triangles). The continuous line histograms are theoretical intranuclear cascade (INCA) cross-sections [17], used as follows: 60.0 MeV (used for 62.7 MeV), 50.0 MeV (for 49.0 MeV), 40.0 MeV (for 41.0 MeV), 35.0 MeV (for 34.5 MeV) and 30.0 MeV (for 31.5 and 28.5 MeV). For all the other incident neutron energies in Figs. 4, 5 the shown histograms result as linear interpolations of the calculated ones. The model in-

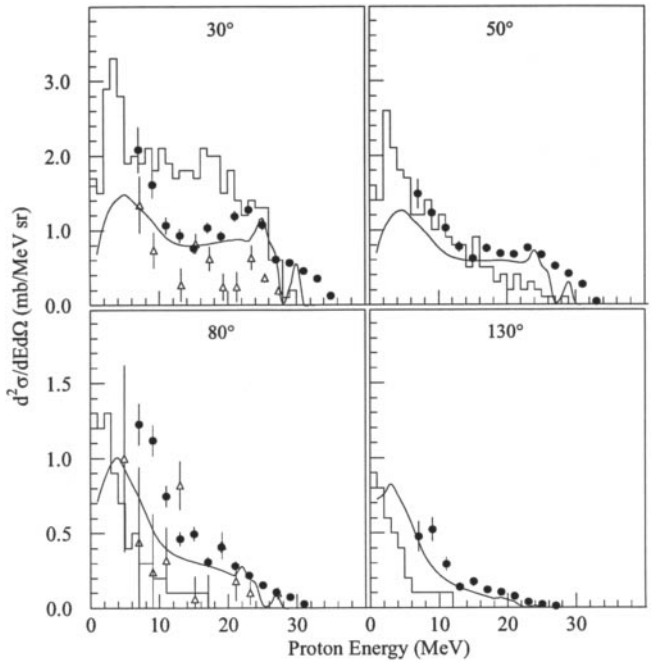

Fig. 6. Measured double-differential cross sections at four lab angles (filled dots in steps of 2 MeV) for ^{16}O(n,px) reactions at 41.0 MeV incident neutron energy. Corresponding data of [16], at 39.7 MeV, are shown as triangles. Our 30° data are compared with 35° data of [16]. Theoretical predictions are from INCA [17] (histograms) and FKK-GNASH [20] (continuous lines)

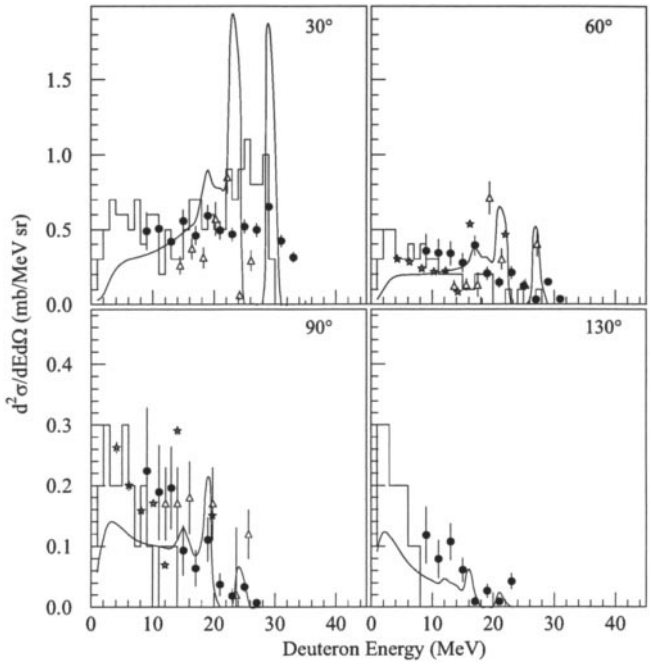

Fig. 7. Same as in Fig. 6 for the case of ^{16}O(n,dx) reactions. Our 30° and 90° data are compared to 35° and 80° data of [16]. Results for ^{16}O(p,dx) reactions at 39.0 MeV [5] are shown as stars

cludes alpha clustering and particle pick-up, followed by Fermi break-up mechanism incorporating decay via intermediate particle-unstable states [17–19].

Within the experimental errors, our data are in fair agreement with data of [16] in Figs. 4, 5.

The theoretically calculated cross-sections of [17] (histograms in Figs. 4, 5) are in good agreement with the experiment for incident neutron energies from 62.7 MeV down to 45.0 MeV, but describe rather poor the shape and the magnitude, for lower incident neutron energies both for protons and deuterons. For the lowest three incident neutron energies in the deuteron case, the theory predicts a huge high energy deuteron peak not observed in the experiment.

Also shown in Figs. 4, 5, at incident neutron energies: 62.7, 49.0, 41.0, 34.5, 31.5 and 28.5 MeV, are the FKK-GNASH calculations [20] (continuous lines) originally done at 60, 50, 40, 35, 30 and 27 MeV. The Feshbach-Kerman-Koonin-GNASH nuclear reaction model code [21] includes Hauser-Feshbach theory for sequential equilibrium decay, preequilibrium (FKK quantum multistep theory or exciton model) and direct reaction mechanisms and uses experimental measurements to optimise the calculations [20]. The code provides a comprehensive description of all important reaction channels. The agreement with the experimental data in Figs. 4, 5 is rather good for incident neutron energies down to 41.0 MeV and fair for lower neutron energies, somewhat better than with the intranuclear cascade model. Nevertheless, it underpredicts the cross sections in the lower energy part of the spectra, specially for lower incident neutron energies. The predicted high energy structure in the deuteron spectra is not observed in our experiment beeing smeared out by a resolution of about 5 MeV, particularly in the case of oxygen where the spectra result from the subtraction of the Al_2O_3 and Al contributions, as explained above.

In Figs. 6, 7 double-differential cross sections, at four different laboratory angles, of the present work are shown for respectively ^{16}O(n,px) and ^{16}O(n,dx) reaction at 41.0 MeV (filled dots). Also shown are experimental data of [16] (triangles) and theoretical calculations from: i) intranuclear cascade model INCA [17] (histograms) and ii) FKK-GNASH nuclear reaction code [20] (continuous lines). In Fig. 7 experimental data for ^{16}O(p,dx) [5] are presented as stars. As previously observed [2–4], INCA predicts, at backward angles, much less high energy particles than kinematically allowed and experimentally observed. It is supposed to be a drawback of the model [2], but it might as well be that the statistics used in the Monte-Carlo simulation in INCA is too poor in order to reproduce the low cross sections in the higher energy ejectile part of the spectra.

For each energy step in the ejectile double-differential spectra, the experimental angular distribution was fitted by a simple two parameter formula [22]: $a \exp(b \cos\theta)$, and then extrapolated to 0° and 180° lab. In this way extrapolated double-differential cross sections are obtained at very forward (2.5° and 10°) and very backward (170° and 177.5°) angles.

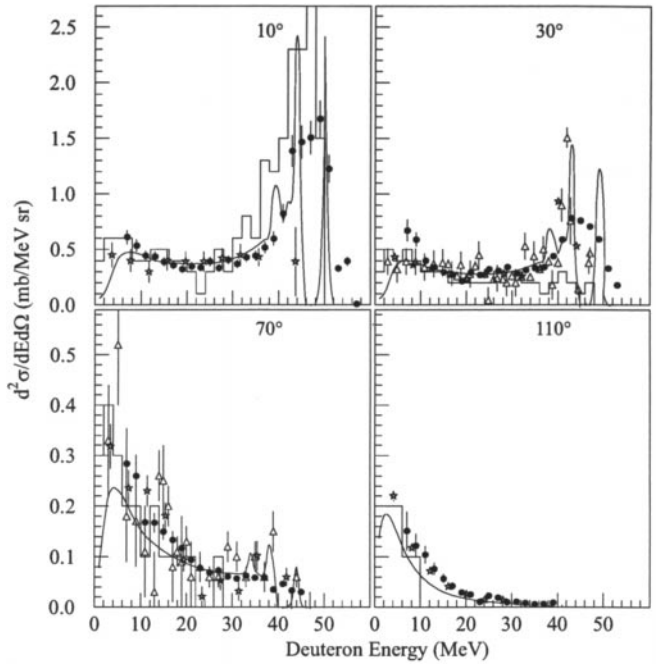

Fig. 8. Experimental double-differential cross sections at four laboratory angles (filled dots in steps of 2 MeV) for ^{16}O(n,dx) reactions at 62.7 MeV incident neutron energy. Corresponding data for ^{16}O(n,dx) [16] (triangles) and for ^{16}O(p,dx) [5] (stars) are shown. Filled dots at 10° lab represent extrapolated cross sections. Our 10°, 30° and 70° data are compared with respectively 12° of [5] and 35° and 65° data of [16]. Theoretical predictions are from INCA [17] (histograms) and GNASH [20] (continuous lines)

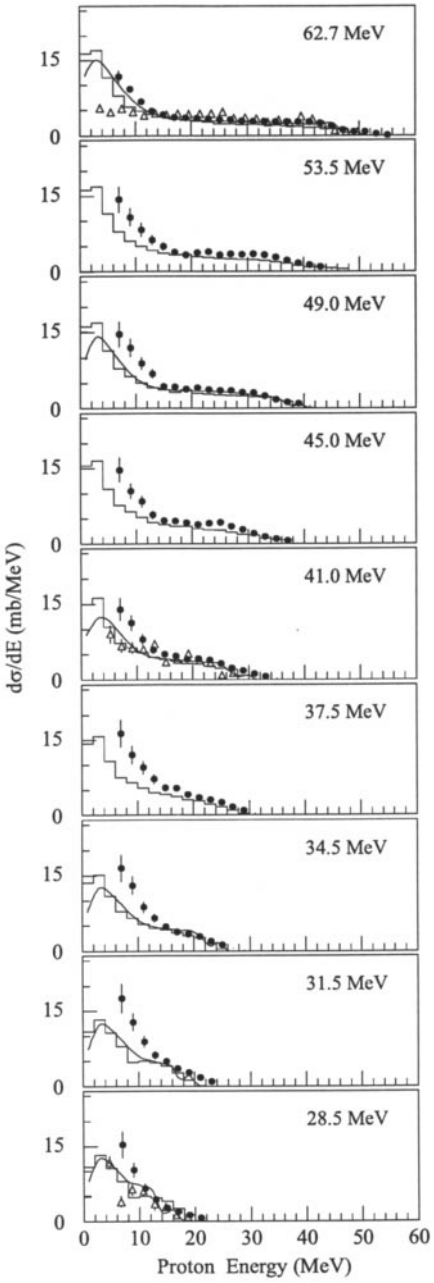

Fig. 9. Energy-differential cross sections (dσ/dE) (in steps of 2 MeV) for ^{16}O(n,px) reactions at the indicated nine incident neutron energies (filled dots). Triangles represent experimental data of [16]. Theoretical predictions are from INCA [17] (histograms) and FKK-GNASH [20] (continuous lines)

Figure 8 presents double-differential cross sections for ^{16}O(n,dx) reactions at 62.7 MeV corresponding to the main peak in the incident neutron energy spectrum. Results of the present work are shown as filled dots (2 MeV steps), stars represent experimental data from proton induced [5] and triangles are data from neutron induced [16] reactions on oxygen. The agreement of the three data sets in Fig. 8 is very good. The filled dots in Fig. 8, at 10° lab are obtained with the above mentioned extrapolation procedure and not the results of direct measurement. The very good accord with experimentally measured data of [5] gives confidence in the extrapolated cross sections. In the energy-differential spectra, the 10° lab double-differential cross sections contribute with about 7% while, the other three extrapolated angles (2.5°, 170° and 177.5°) with less than 2% of the total. Theoretical calculations in Fig. 8 are from INCA [17] (histograms) and GNASH [20] (continuous lines). GNASH describes very well the spectra in Fig. 8. INCA describes well the forward angle data but predicts, for higher lab angles, much less cross sections than experimentally measured at higher ejectile energies.

For each incident neutron energy, by angle integration of the measured energy spectra angular distribution, energy-differential cross sections (dσ/dE) are obtained. Figs. 9, 10 show respectively for protons and deuterons these cross sections (steps of 2 MeV) vs the incident neutron energy. The spectra in Figs. 9, 10 include the extrapolated double-differential cross sections at very forward and very backward angles. The meaning of the symbols is the same as in figures above. The agreement of the present experimental data and those of [16] is good. The INCA and FKK-GNASH theoretical calculations for protons agree between themselves and both underpredict the lower energy part of each spectrum. For lower incident neutron energies in the deuteron spectra, the GNASH predictions

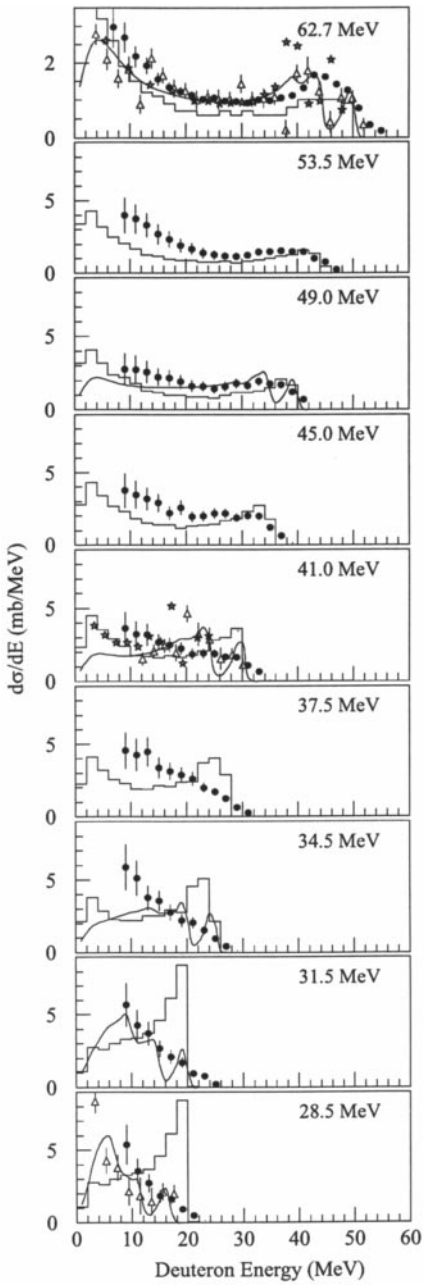

Fig. 10. Same as in Fig. 9 for the case of ^{16}O(n,dx) reaction. The stars at 62.7 and 41.0 MeV are experimental data at respectively 61.5 and 39.0 MeV for ^{16}O(p,dx) reactions [5]

compared to INCA calculations, are in better accord with the experimental data. For deuterons in Fig. 10, the stars at 62.7 and 41.0 MeV incident neutron energies represent data for ^{16}O(p,dx) reaction [5] at respectively 61.5 and 39.0 MeV incident proton energy. They agree well with present data, the differences resulting from different Q-values ($Q_{(n,d)} = -9.9$ MeV, $Q_{(p,d)} = -13.4$ MeV) and the structure in the high energy part of the spectra seen in the proton induced reactions due to the better energy resolution.

The intranuclear cascade model is based on free nucleon-nucleon scattering for which the experimental cross sections are parametrised and used [2]. Therefore, the model is supposed to work at incident nucleon energies of 100 MeV or more. Nevertheless good results have been obtained for lower incident neutron energies (61.0 and 39.7 MeV) [2]. At the incident neutron energies reported in the present work (62.7 MeV down to 28.5 MeV) for proton emission, the breaking of the free nucleon-nucleon scattering condition, specially for incident neutron energies lower than 40 MeV, might explain the differences observed in Fig. 9 between the experimental and the theoretical data. Small amounts of energy transfered to the nucleons in the nucleus from the incident neutron, on its way to the scattering place, will increase the emission of predominantly low energy protons as seen in Fig. 9. On the same base, one can explain, specially for lower incident neutron energies, the differences between the experiment and the intranuclear cascade model which predicts steeper than experimentally observed, angular distributions (Figs. 4, 6). In Figs. 5, 10 the high energy deuteron peak is theoretically predicted based on an analytical formula [2] as the result of the plane wave Born approximation, giving a very crude estimation of the (n,d) pick-up process, which is inadequate for lower incident neutron energies.

Figures 11, 12 present angle-differential cross sections ($d\sigma/d\Omega$) (filled dots), resulting by energy integration of the measured energy spectra for each incident neutron energy. The triangles are angle-differential cross sections from the integration of the energy spectra for 2.5°, 10°, 170° and 177.5° lab angles which were extrapolated from the measured angular distributions. The lines in Figs. 11, 12 are to guide the eye.

Table 1 gives total cross sections for proton emission resulting from the integration of the energy-differential cross sections in Fig. 9, together with the theoretical predictions based on INCA [17] and FKK-GNASH [20] model calculations. For both theories, predicted cross sections

Table 1. Experimentally measured total cross-sections (mb) of this work, for proton emission induced by fast neutrons on oxygen. Theoretical values from [17] and [20] are given for above and, in parenthesis, below the experimental low energy threshold (6 MeV). Some of the indicated theoretical values result from a linear interpolation of the calculated ones

E_n (MeV)	σ(n,px) (mb) (this work)	σ(n,px) (mb) [17]	σ(n,px) (mb) [20]
62.7 ± 2.0	168 ± 9	123 (90)	148 (75)
53.5 ± 2.5	171 ± 24	118 (89)	136 (71)
49.0 ± 2.0	165 ± 22	112 (89)	124 (68)
45.0 ± 2.0	153 ± 20	102 (86)	112 (65)
41.0 ± 2.0	141 ± 18	91 (84)	100 (62)
37.5 ± 1.5	144 ± 20	85 (82)	95 (61)
34.5 ± 1.5	127 ± 18	79 (80)	90 (60)
31.5 ± 1.5	119 ± 17	64 (70)	70 (59)
28.5 ± 1.5	86 ± 16	64 (70)	61 (61)

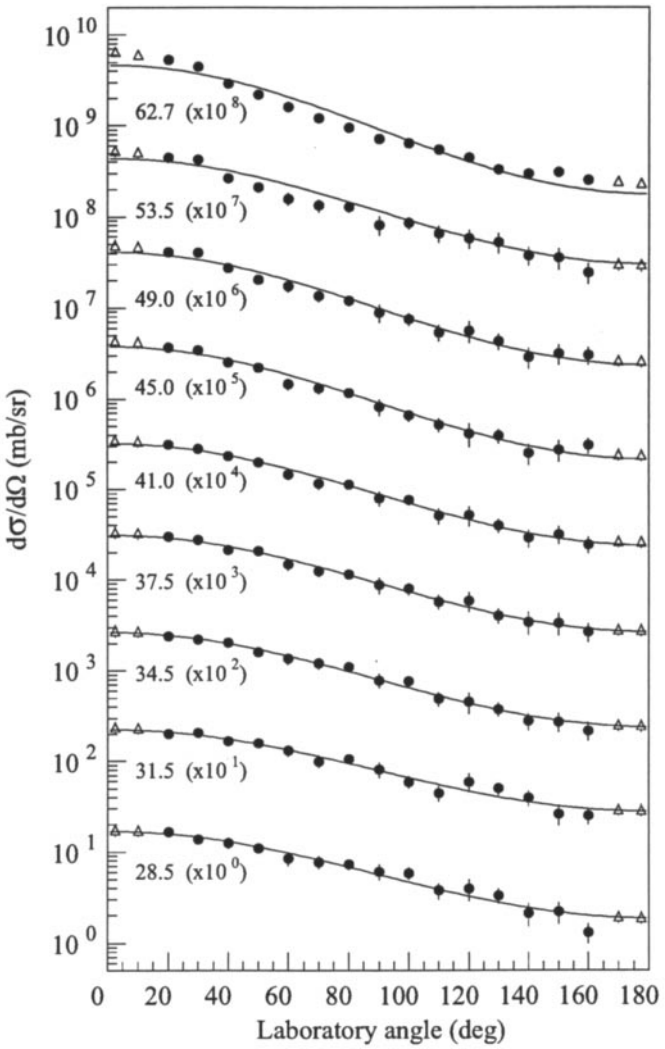

Fig. 11. Experimental angle-differential ($d\sigma/d\Omega$) cross sections for proton emission at the indicated nine incident neutron energies (filled dots). The triangles represent the extrapolation of the experimental data. In parenthesis there are scale factors as decades. The lines serve to guide the eye. The experimental low energy threshold is 6 MeV

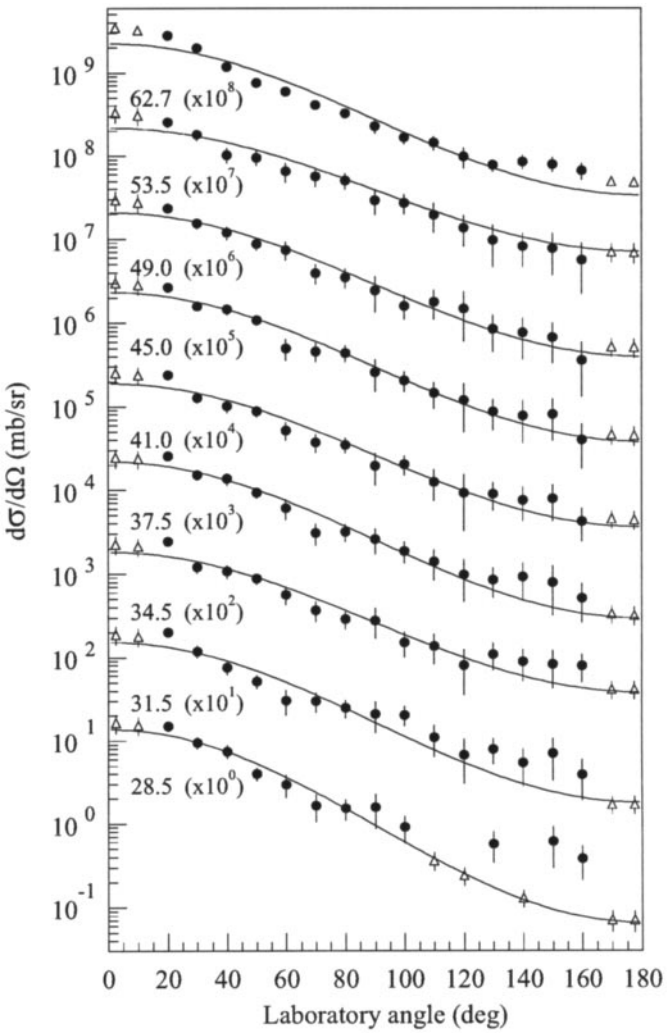

Fig. 12. Same as in Fig. 11 for the case of deuterons. The experimental low energy threshold is 6 MeV for 62.7 MeV data and 8 MeV for all the rest

under and above the experimental low energy cuts in the spectra are indicated. Table 2 has the same meaning as Table 1 but for deuterons. Theoretical estimations of the total cross sections from both models, underestimate the experimental values. Both theories agree between themselves within less than 10% in the total cross sections for protons over the entire ejectiles energy range. For deuterons, the dependence of the total cross sections on the incident neutron energy in GNASH calculations, confirms the trend of the experimental data. The INCA predictions show a slow increase of the deuteron total cross sections with decreasing incident neutron energy. This behaviour might result from the contribution of the huge high energy deuteron peak, not seen in the experiment, but predicted at forward angles in the double-differential cross sections of [17] for lower incident neutron energies (Fig. 5).

Table 2. Experimentally measured total cross-sections (mb) of this work, for deuteron emission induced by fast neutrons on oxygen. Theoretical values from [17] and [20] are given for above and, in parenthesis, below the experimental low energy threshold (6 MeV for 62.7 data and 8 MeV for all the rest). Some of the indicated theoretical values result from a linear interpolation of the calculated ones

E_n (MeV)	σ(n,px) (mb) (this work)	σ(n,px) (mb) [17]	σ(n,px) (mb) [20]
62.7 ± 2.0	65 ± 6	42 (23)	54 (12)
53.5 ± 2.5	70 ± 16	42 (24)	54 (13)
49.0 ± 2.0	64 ± 15	42 (26)	53 (14)
45.0 ± 2.0	68 ± 14	45 (26)	51 (13)
41.0 ± 2.0	57 ± 12	48 (27)	49 (12)
37.5 ± 1.5	63 ± 13	51 (24)	46 (13)
34.5 ± 1.5	57 ± 12	54 (22)	43 (14)
31.5 ± 1.5	44 ± 10	59 (19)	32 (23)
28.5 ± 1.5	33 ± 8	59 (19)	19 (31)

5 Conclusions

We report, in the present paper, a consistent experimental data set for proton and deuteron emission induced by fast neutrons on oxygen, covering at nine energies, the important incident neutron energy range 25 to 65 MeV.

Experimental proton and deuteron emission double-differential cross sections ($d^2\sigma/d\Omega dE$) resulting from the interaction of fast neutrons on oxygen are reported.

Angular distributions were measured at 15 laboratory angles between 20° and 160°. Starting from the experimental angular distributions of the energy spectra, reliable extrapolations are done for double-differential cross sections in the very forward (2.5° and 10°) and in the very backward direction (170° and 177.5°).

The double-differential cross sections of the present work are in good (for 62.7 MeV) and fair (for 41.0 and 28.5 MeV incident neutron energies) agreement with previous measurements for neutron induced reactions on oxygen [16]. In the deuteron case, there is a good agreement with data from proton induced emission on oxygen [5]. Theoretical predictions resulting from the intranuclear cascade model INCA [17] and the FKK-GNASH nuclear model code [20] are also considered. Generally both theories describe rather well the magnitude and the shape of the experimental spectra for higher incident neutron energies. For incident energies less than 41.0 MeV the INCA calculations overpredict, both for protons and deuterons, the experimental data at forward angles. In the backward hemisphere INCA predicts, for higher ejectile energies, less cross section than experimentally measured. The GNASH code gives a better estimation of the magnitude and shape of the experimental spectra.

Energy-differential cross-sections ($d\sigma/dE$) are deduced from our measured double-differential cross sections for all reported incident neutron energies. Overall, they compare rather well with previously reported data [16] and in the case of deuterons with data from proton induced reactions on oxygen [5].

Angle-differential ($d\sigma/d\Omega$) and experimental total cross sections (σ_T) are also presented for all the nine incident neutron energies.

Only an illustrative selection of detailed results has been presented here. Complete double-differential production cross sections and their angular distributions may be obtained from Mrs. S. Benck.

We would like to thank the Louvain-la-Neuve Cyclotron staff for permanent assistance and quality of the beam. We acknowledge support of the Institut Interuniversitaire des Sciences Nucleaires, Belgium and partly the European Economic Community (contract FI3P-93-0084-BE). Thanks are due to M. B. Chadwick for providing detailed numerical values of [20].

References

1. T. S. Subramanian, J. L. Romero, F. P. Brady, Nucl. Instrum. Methods **174**, 475 (1980)
2. T. S. Subramanian, J. L. Romero, F. P. Brady, J. W. Watson, D. H. Fitzgerald, R. Garett, G. A. Needham, J. L. Ullmann, C. I. Zanelli, D. J. Brenner and R. E. Prael, Phys. Rev. **C28**, 521 (1983)
3. I. Slypen, V. Corcalciuc, J. P. Meulders, Phys. Rev. **C51**, 1303 (1995)
4. I. Slypen, V. Corcalciuc, J. P. Meulders and M. Chadwick, Phys. Rev. **C53**, 1309 (1996)
5. F. E. Bertrand and R. W. Peelle, Phys. Rev. **C8**, 1045 (1973); F. E. Bertrand and R. W. Peelle, Oak Ridge Report, ORNL-4799 (1973)
6. A. S. Meigooni, J. S. Petler, R. W. Finlay, Phys. Med. Biol. **29**, 643 (1984)
7. I. Slypen, V. Corcalciuc, J. P. Meulders, Phys. Med. Biol. **40**, 73 (1995)
8. A. Bol, P. Leleux, P. Lipnik, P. Macq, A. Ninane, Nucl. Instrum. Methods **214**, 169 (1983)
9. C. Dupont, P. Leleux, P. Lipnik, P. Macq, A. Ninane, Nucl. Instrum. Methods **A256**, 169 (1983)
10. I. Slypen, V. Corcalciuc, A. Ninane and J. P. Meulders, Nucl. Instrum. Methods **A337**, 431 (1994)
11. F. Bernachi, B. Chambon, B. Cheynis, D. Drain, C. Pastor, D. Seghier, K. Zaid, A. Giorni, D. Heuer, A. Leres, C. Morand, P. Stassi and J. B. Viano, Nucl. Instrum. Methods **A281**, 137 (1989)
12. J. Alarja, A. Dauchy, A. Giorni, C. Morand, E. Pollaco, P. Stassi, R. Billery, B. Chambon, B. Cheynis, D. Drain and C. Pastor, Nucl. Instrum. Methods **A242**, 352 (1986)
13. I. Slypen, V. Corcalciuc and J. P. Meulders, Rom. Journal Phys. vol 38, **No 4-6** (1993)
14. S. Benck, I. Slypen, V. Corcalciuc and J. P. Meulders, Nucl. Phys. **A615**, 220 (1997)
15. I. Slypen, V. Corcalciuc and J. P. Meulders, Nucl. Instrum. Methods **B88**, 275 (1994)
16. T. S. Subramanian, J. L. Romero, F. P. Brady, D. H. Fitzgerald, R. Garett, G. A. Needham, J. L. Ullmann, J. W. Watson, C. I. Zanelli, D. J. Brenner and R. E. Prael, Phys. Rev. **C34**, 1580 (1986); J. L. Romero, private communication (1994)
17. D. J. Brenner and R. E. Prael, Atomic and Nucl. Data Tables **41**, 71 (1989)
18. K. Chen, Z. Fraenkel, G. Friedlander, J. R. Groves, J. M. Miller and Y. Shimamato, Phys. Rev. **166**, 949 (1968)
19. G. J. Mathews, B. G. Glagola, R. A. Moyle and V. E. Viola Jr., Phys. Rev. **C25**, 2181 (1982)
20. M. B. Chadwick, P. G. Young, Nucl. Sci. Eng. **123**, 1 (1996); M. B. Chadwick, Private communication to S. Benck
21. P. G. Young, E. D.. Arthur and M. B. Chadwick, Los Alamos National Laboratory report LA-MS-12343 (1992)
22. C. Kalbach, Phys. Rev. **C34**, 2350 (1988)